

# Cortical Synaptic AMPA Receptor Plasticity during Motor Learning

## Highlights

- *In vivo* imaging of AMPA receptors reveals high dynamics at individual synapses
- Motor learning induces potentiation of a clustered subset of dendritic spines
- Motor learning increases AMPA receptor levels in motor and visual cortex
- Plasticity of visual cortex during learning depends on visual input

## Authors

Richard H. Roth, Robert H. Cudmore,  
Han L. Tan, Ingie Hong, Yong Zhang,  
Richard L. Huganir

## Correspondence

[rughanir@jhmi.edu](mailto:rughanir@jhmi.edu)

## In Brief

Through *in vivo* imaging of synaptic AMPA receptors in mice, Roth et al. show that motor learning potentiates synapses in both motor and visual cortex. Recruitment and potentiation of the visual cortex require visual stimuli during motor training.



# Cortical Synaptic AMPA Receptor Plasticity during Motor Learning

Richard H. Roth,<sup>1</sup> Robert H. Cudmore,<sup>2</sup> Han L. Tan,<sup>1</sup> Ingie Hong,<sup>1</sup> Yong Zhang,<sup>3</sup> and Richard L. Huganir<sup>1,4,\*</sup>

<sup>1</sup>Solomon H. Snyder Department of Neuroscience and Kavli Neuroscience Discovery Institute, Johns Hopkins University School of Medicine, Baltimore, MD 21205, USA

<sup>2</sup>Department of Physiology and Membrane Biology, University of California School of Medicine, Davis, CA 95616, USA

<sup>3</sup>Department of Neurobiology, School of Basic Medical Sciences and Neuroscience Research Institute, Key Lab for Neuroscience, Ministry of Education of China and National Health Commission of the P.R. China, IDG/McGovern Institute for Brain Research at PKU, Peking University, Beijing 100191, China

<sup>4</sup>Lead Contact

\*Correspondence: rhuganir@jhmi.edu

<https://doi.org/10.1016/j.neuron.2019.12.005>

## SUMMARY

Modulation of synaptic strength through trafficking of AMPA receptors (AMPARs) is a fundamental mechanism underlying synaptic plasticity, learning, and memory. However, the dynamics of AMPAR trafficking *in vivo* and its correlation with learning have not been resolved. Here, we used *in vivo* two-photon microscopy to visualize surface AMPARs in mouse cortex during the acquisition of a forelimb reaching task. Daily training leads to an increase in AMPAR levels at a subset of spatially clustered dendritic spines in the motor cortex. Surprisingly, we also observed increases in spine AMPAR levels in the visual cortex. There, synaptic potentiation depends on the availability of visual input during motor training, and optogenetic inhibition of visual cortex activity impairs task performance. These results indicate that motor learning induces widespread cortical synaptic potentiation by increasing the net trafficking of AMPARs into spines, including in non-motor brain regions.

## INTRODUCTION

AMPA-type glutamate receptors (AMPARs) mediate the majority of fast excitatory synaptic transmission in the brain, and regulation of synaptic AMPAR levels is a fundamental mechanism modulating synaptic strength. Increases in AMPAR levels at dendritic spines, where the majority of excitatory synapses are located, underlie processes that increase synaptic strength, such as long-term potentiation (LTP), and decreases in AMPAR levels mediate processes that decrease synaptic strength, such as long-term depression (LTD) (Bredt and Nicoll, 2003; Diering and Huganir, 2018; Huganir and Nicoll, 2013; Kessels and Malinow, 2009; Malinow and Malenka, 2002). Trafficking of AMPARs into and out of synapses is a highly dynamic process involving endosomal trafficking and lateral diffusion along the plasma membrane (Choquet, 2018; Henley et al., 2011; Roth et al.,

2017). Disruption of proper AMPAR function or trafficking impairs synaptic plasticity and consequently, higher brain functions such as learning and memory (Volk et al., 2015). Despite the importance of AMPAR regulation during learning and memory, the time course and spatial organization of AMPAR trafficking *in vivo* during learning have not been described.

Previous studies in mice have demonstrated that motor learning can induce synaptic plasticity in the motor cortex, during which overall synaptic connections are strengthened through an LTP-like mechanism (Rioult-Pedotti et al., 1998, 2000). More recent *in vivo* imaging studies have shown that motor-learning-induced plasticity involves a significant increase in the formation and elimination of dendritic spines (Fu et al., 2012; Xu et al., 2009; Yang et al., 2009) as well as enlargement of a subset of existing spines (Hayashi-Takagi et al., 2015). Furthermore, artificially weakening learning-related spines *in vivo* impairs learned motor behavior (Hayashi-Takagi et al., 2015). Taken together, these studies suggest that synaptic plasticity in the motor cortex plays an important role in the acquisition of motor skills. However, we still lack an understanding of the spatiotemporal dynamics of synaptic plasticity during learning, and how changes in synaptic AMPAR levels correlate with learning is largely unknown.

To address this knowledge gap, we used *in vivo* two-photon imaging of fluorescently labeled AMPARs to resolve the spatial and temporal patterns of AMPAR trafficking during learning (Roth et al., 2017; Zhang et al., 2015). We trained mice on a forelimb reaching motor task and repeatedly imaged surface expression levels of the AMPAR subunit GluA1 on the same dendritic segments of layer 5 neurons in the motor cortex over the course of learning. Motor learning induced a net increase in spine GluA1 levels that correlated with increased reaching performance and persisted beyond the end of training. Although globally there was a significant increase, the amount of GluA1 in individual spines was highly dynamic, with some spines showing increases and others showing decreases in GluA1 during learning. Unexpectedly, we also observed strong increases in spine GluA1 levels in neurons of the visual cortex of mice learning the motor reaching task. Our results reveal the spatial and temporal dynamics of synaptic AMPAR plasticity underlying learning and demonstrate the involvement of plasticity in visual and motor regions of the cortex during motor learning.



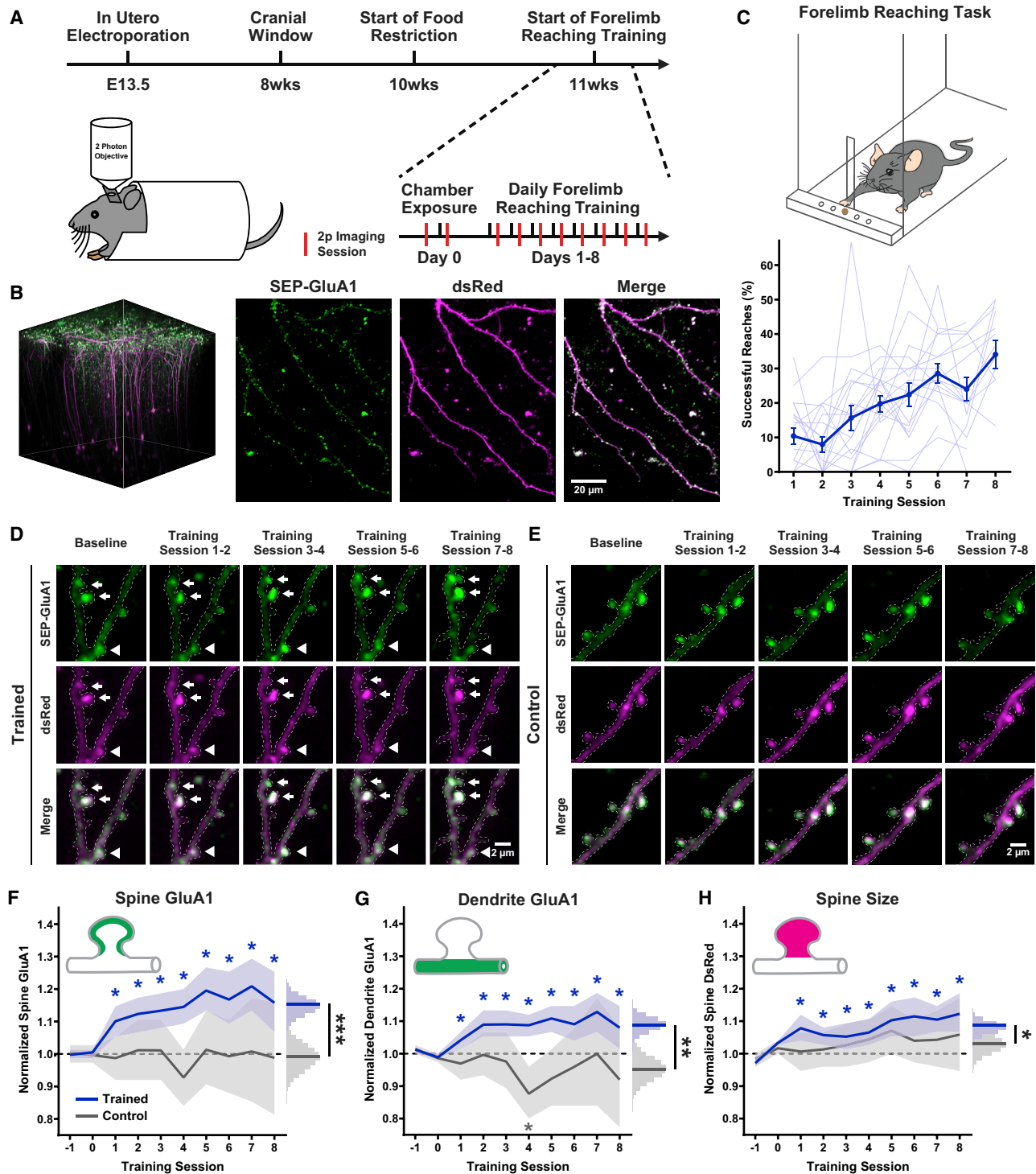


**Figure 1. Daily Skilled Motor Learning Induces Increases in Spine GluA1 Levels**

(A) Experimental timeline with schematic drawing of *in vivo* two-photon imaging.

(B) Representative imaging volume of sparsely labeled layer 5 neurons in the motor cortex expressing SEP-GluA1 (green), myc-GluA2, and dsRed (magenta). Left, 3D reconstruction; right, maximum intensity projections of apical dendrites.

(C) Schematic drawing of forelimb reaching task (top) and behavioral performance of mice trained on forelimb reaching task (bottom). Thin lines represent individual mice and the bold line is the average. n = 20. Error bars, SEM.

(legend continued on next page)

## RESULTS

### Motor Learning Induced a Long-Lasting Increase in Spine GluA1 Levels in Motor Cortex

To monitor dynamic levels of spine AMPARs *in vivo*, we used longitudinal two-photon microscopy to image fluorescently tagged AMPARs in mice. We sparsely transfected layer 5 neurons by *in utero* electroporation with constructs encoding the AMPAR subunit GluA1 tagged with Super-Ecliptic pHluorin (SEP) (Miesenböck et al., 1998), myc-GluA2, and dsRed, allowing the visualization of GluA1-containing AMPARs as well as neuronal morphology (Figure S1) (Roth et al., 2017; Zhang et al., 2015). Expression of exogenous SEP-GluA1 and myc-GluA2 did not significantly affect synaptic properties such as amplitude and frequency of miniature excitatory postsynaptic currents (mEPSCs) (Figure S2). Once electroporated mice reached young adulthood, we implanted a cranial window over the motor cortex for *in vivo* two-photon imaging (Figures 1A and 1B). Following a 2–3 week recovery period, we trained mice on a forelimb reaching task, which required freely moving mice to use a single paw to reach for a small food pellet through a slit opening in the training chamber. For training, mice were food deprived for 5–7 days, familiarized with the training chamber (for details, see STAR Methods), and then trained daily for 8 days. During the training period, mice showed progressive improvement in the rate of successfully retrieved food pellets without dropping (Figure 1C and Video S1). The primary motor cortex was imaged repeatedly, twice following baseline sessions during chamber familiarization, and then daily after each training session.

We first examined layer 5 neurons in the motor cortex, where previous studies had described structural plasticity as a result of motor learning (Fu et al., 2012; Rioult-Pedotti et al., 1998; Xu et al., 2009). We quantified spine-surface GluA1 levels on apical dendrites by normalizing the mean SEP fluorescence in spines to the mean dsRed fluorescence on the adjacent dendritic shaft (Figure S3A). Dendritic shaft dsRed fluorescence was stable over the experimental time period, making it a reliable normalization factor for small variations in daily imaging conditions (Figures S3B and S3C). Through repeated imaging of the same neurons and synapses during motor learning, we observed that, on average, GluA1 levels in spines of layer 5 motor cortex neurons progressively increased over time (Figures 1D, 1F, and S5A–B). Control mice that did not undergo training, but were food restricted and exposed to the training chamber, did not show this increase (Figures 1E, 1F, S5A, and S5C). We further compared GluA1 levels in the motor cortex contralateral or ipsilateral to the trained paw by imaging the left hemisphere of mice

either trained on their left or right paw (Figures S4A–S4C) and observed that spine GluA1 increases in both contralateral and ipsilateral motor cortex (Figure S4D and S4E). Since we found no significant differences between the two hemispheres, we combined both groups of trained mice for further analysis.

In addition to spine GluA1 levels, we also analyzed GluA1 levels on the dendritic shaft adjacent to spines and again found a small but significant increase during learning (Figure 1G), which is consistent with existing models of LTP where long-lasting potentiation occurs through AMPAR insertion into the dendritic shaft around potentiated synapses and lateral diffusion of extra-synaptic AMPARs to synapses (Lin et al., 2009; Makino and Malinow, 2009; Yudowski et al., 2007). Accordingly, the changes in GluA1 levels of individual spines were strongly correlated with the GluA1 changes in their adjacent dendritic shaft (Figure S5D). Since synaptic potentiation is also linked to increases in the size of dendritic spines (Bosch and Hayashi, 2012; Matsuzaki et al., 2004), we measured spine size changes during learning by quantifying dsRed fluorescence intensity and observed a small but significant increase (Figure 1H). The increase in spine size was strongly correlated with changes in spine GluA1 and had a weaker correlation to changes in dendritic GluA1 (Figures S5E and S5F). To exclude any potential confounding effects of daily anesthesia during imaging, we trained a cohort of mice on the forelimb reaching task, but only imaged during baseline sessions and at the end of training (Figure S5G). In these animals, spine and dendrite GluA1 were also increased following motor learning (Figures S5H–S5J).

### Correlation of Spine GluA1 Levels in Motor Cortex with Reaching Performance

Comparing daily spine GluA1 levels of trained mice to their task performance on any given day showed a positive correlation between average spine AMPAR levels and reaching success rates (Figure 2A). Whereas the correlation did not reach statistical significance for all individual mice, the majority of mice showed a trend toward a positive slope (Table S1). Given the variability in individual behavioral and spine GluA1 data at any given day, the low statistical significance of individual regression lines for each mouse is not surprising. However, the strong positive correlation of daily averages shows that in trained mice reaching performance and spine GluA1 levels increased in a correlated manner. To assess whether mice that showed a steeper learning curve on the forelimb reaching task also showed a larger increase in spine GluA1 levels, we compared the slope of average GluA1 dynamics of each individual mouse with the slope of its learning curve (Figure 2B). We found a positive correlation, revealing that mice that showed more improvement during motor

(D) Representative images of spines on layer 5 apical dendrites in trained mice across training sessions. Arrows indicate spines with gradually increasing SEP-GluA1 signal intensity; arrow heads indicate a spine with a transient increase in SEP-GluA1.

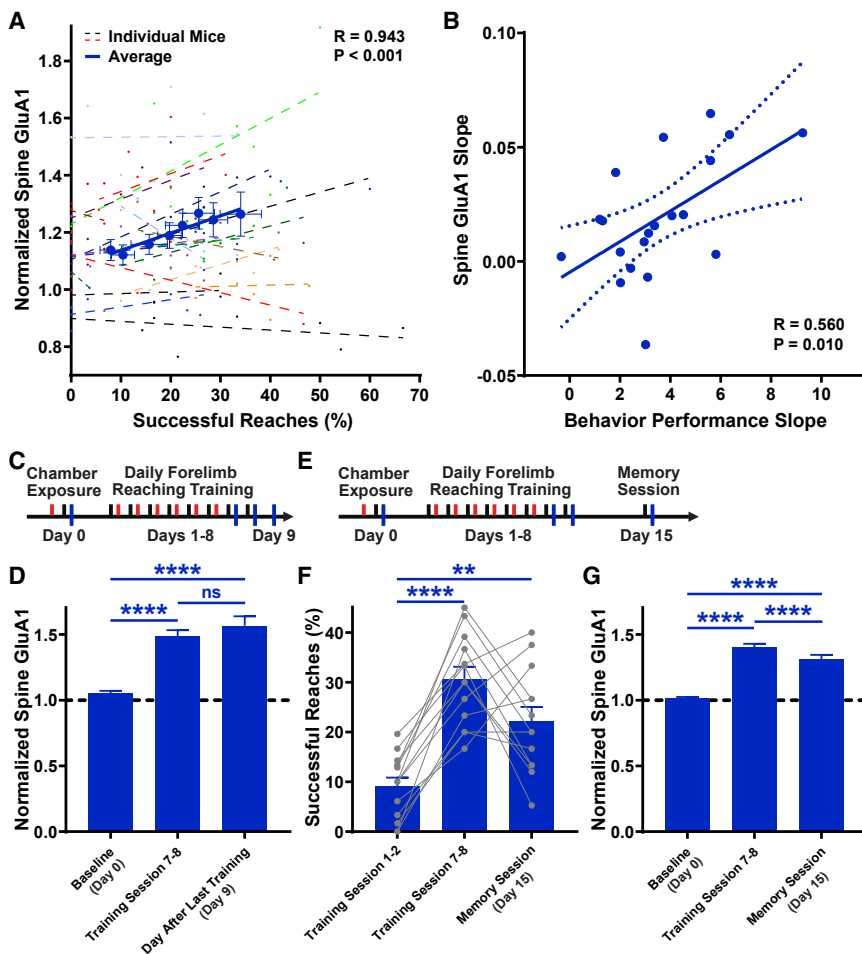
(E) Representative images of spines on layer 5 apical dendrites in control mice (exposed to the training chamber without reaching) across training sessions.

(F) Average spine GluA1 intensity normalized to baseline levels in trained (blue) and control (gray) mice over the course of motor learning.

(G) Average GluA1 intensity in the dendritic shaft of trained (blue) and control (gray) mice.

(H) Average spine dsRed intensity of trained (blue) and control (gray) mice.

(F–H) Line represents average across  $n = 74$  dendrites with 1781 spines from 20 mice (trained) and  $n = 24$  dendrites with 411 spines from 9 mice (control). Shading depicts bootstrapped 95% confidence intervals (see STAR Methods). \* $p < 0.05$  indicates significant difference of mean fluorescence signal intensity from baseline. Right histograms represent distribution of bootstrapped mean values during training. \*\* $p < 0.05$ , \*\*\* $p < 0.01$ , \*\*\*\* $p < 0.001$  indicate significant mean difference between groups.



(G) Average spine GluA1 intensity at baseline, average of training session 7 and 8, and after memory session. Only spines that increased in GluA1 levels during learning were included (average GluA1 at training session 7 and 8 was larger than baseline). n = 351 spines. Error bars, SEM. \*\*\*p < 0.0001, Friedman test with Dunn's multiple comparison test.

training also gained a greater amount of spine AMPARs over the course of training.

To assess the possibility that the observed increase in spine GluA1 levels was a result of increased motor activity during the training session right before each imaging session, a subset of trained mice was imaged for one additional day following the last day of training (Figure 2C). At this time point, mice were well trained and possessed the learned motor skill memory but had not performed the task immediately before imaging. In spines that showed an increase in GluA1 during the eight days of training, we found that GluA1 levels remained increased one day after the last training (Figure 2D).

To further examine the link between spine GluA1 levels and mouse task performance, we probed motor task performance in a subset of mice one week following the last training day and imaged them after this 'memory session' (Figure 2E). At this time point, mice retained the high levels of reaching performance, indicating retention of motor skill memory (Figure 2F). Spines that showed a GluA1 increase during initial learning also

retained their increase following this memory session (Figure 2G). These observations that spine GluA1 levels remain elevated after motor training underline the role of AMPAR plasticity during long-term motor learning.

#### Diverse Patterns of GluA1 Dynamics in Individual Spines

Although there was an increase in the average GluA1 content of all spines during motor learning, we took advantage of the spatiotemporal resolution offered by *in vivo* imaging to ask whether individual spines of layer 5 neurons in the motor cortex showed the same direction and degree of change, or whether there is diversity in the AMPAR dynamics of individual spines. Surprisingly, we found that GluA1 content at individual spines was quite dynamic. In both trained and control mice, there were spines that displayed an increase in their GluA1 levels, spines that showed a decrease, and spines with stable GluA1 levels during the training or chamber exposure period (Figures 3A and 3B). However, the distribution of GluA1 changes in spines was significantly shifted toward larger increases in trained mice (Figure 3C). We further classified spine

**Figure 2. Spine GluA1 Levels Correlate with Increased Behavioral Performance**

(A) Correlation of reaching performance and spine GluA1 levels at individual training sessions. Small symbols represent individual mice, and dashed lines are linear regressions for each mouse. Bold blue symbols represent average GluA1 levels and behavioral performance of n = 20 mice at each training session. Bold blue line is the linear regression for the average values. Error bars, SEM.

(B) Correlation between slope of reaching performance learning curve and slope of spine GluA1 time course for individual mice. Line represents linear regression with 95% confidence interval (dotted lines). n = 20 mice.

(C) Experimental timeline for imaging 24 h after last training day. Imaging sessions (red) that data in (D) is plotted from are indicated by blue lines.

(D) Average spine GluA1 intensity at baseline, average of training session 7 and 8, and 24 h after last training day. Only spines that increased in GluA1 levels during learning were included (average GluA1 at training session 7 and 8 was larger than baseline). n = 147 spines. Error bars, SEM ns, not significant, \*\*\*p < 0.0001, Friedman test with Dunn's multiple comparison test.

(E) Experimental timeline for reaching performance testing and imaging 1 week after last training day. Imaging sessions (red) that data in (G) is plotted from are indicated by blue lines.

(F) Behavioral performance of mice at the beginning of training (average of sessions 1 and 2), end of daily training (average of sessions 7 and 8), and 1 week after the last training day (memory session). n = 13 mice. Error bars, SEM ns, not significant, \*\*p < 0.01, \*\*\*p < 0.0001, Friedman test with Dunn's multiple comparison test.

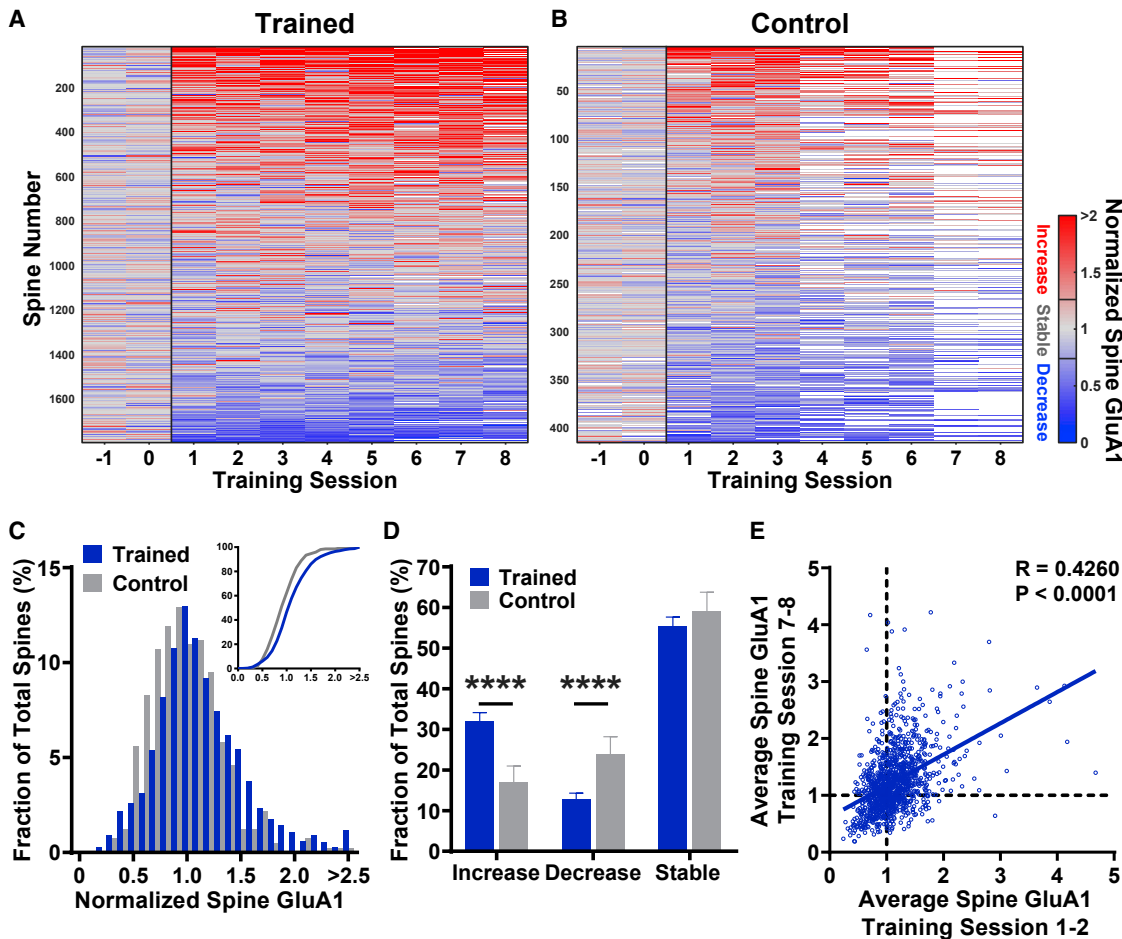


**Figure 3. Diverse Synaptic GluA1 Plasticity Between Individual Spines**

(A) Heatmap showing amount of spine GluA1 in individual spines of trained mice. Each row represents a single spine. The GluA1 level of each spine is normalized to its average baseline levels and rows are sorted by average GluA1 change during motor learning. n = 1781 spines.

(B) Same as (A) showing heatmap of individual spines for control mice. n = 411 spines.

(C) Distribution histogram and cumulative distribution (inset) of average GluA1 change during motor learning. p < 0.0001 (Two-sample Kolmogorov-Smirnov test).

(D) Fraction of spines showing an average increase (>26% increase over baseline), decrease (>26% decrease), or being stable (<26% change) during learning. Error bars, 95% confidence intervals. \*\*\*p < 0.0001, chi-square test with Bonferroni correction.

(E) Comparison of GluA1 change in early training sessions (average of training sessions 1 and 2) and late training sessions (average of training sessions 7 and 8) with linear fits. n = 1154 spines.

as increasing, decreasing, or stable based on their average fold change during learning (see [STAR Methods](#)) and noticed a larger fraction of spines with increasing GluA1 levels as well as a smaller fraction of spines with decreasing GluA1 levels in trained mice compared to non-trained control mice ([Figure 3D](#)).

To determine whether the dynamics we observed in non-trained control mice were due to restricted access to food or exposure to the training chamber, we imaged naive mice that had only experienced their home cage with free access to food. Again, we observed diverse changes in individual spine GluA1 levels over 10 days in home cage control mice, while the average GluA1 levels remained stable ([Figure S6A–S6F](#)). In all three groups (trained, control, home cage control) the degree of green fluorescence change in spine ROIs was

significantly larger than in the associated background regions ([Figures S6G–S6I](#)).

We noticed that, in addition to the spines that showed increasing GluA1 levels from early on during the training ([Figure 1D](#), arrows), there were also spines that showed transient increases in GluA1 levels ([Figure 1D](#), arrow head). The increase in GluA1 we observed on average could be either driven by gradually increasing spines or by an increasing number of spines with transiently increasing GluA1 levels. To distinguish between these two possibilities, we compared spine GluA1 changes following early training sessions with spine GluA1 changes following late training sessions ([Figure 3E](#)). We found a positive correlation, indicating that spines showing an increase at the beginning of training further increased during later training sessions, supporting the idea that the average increase in spine GluA1 levels was

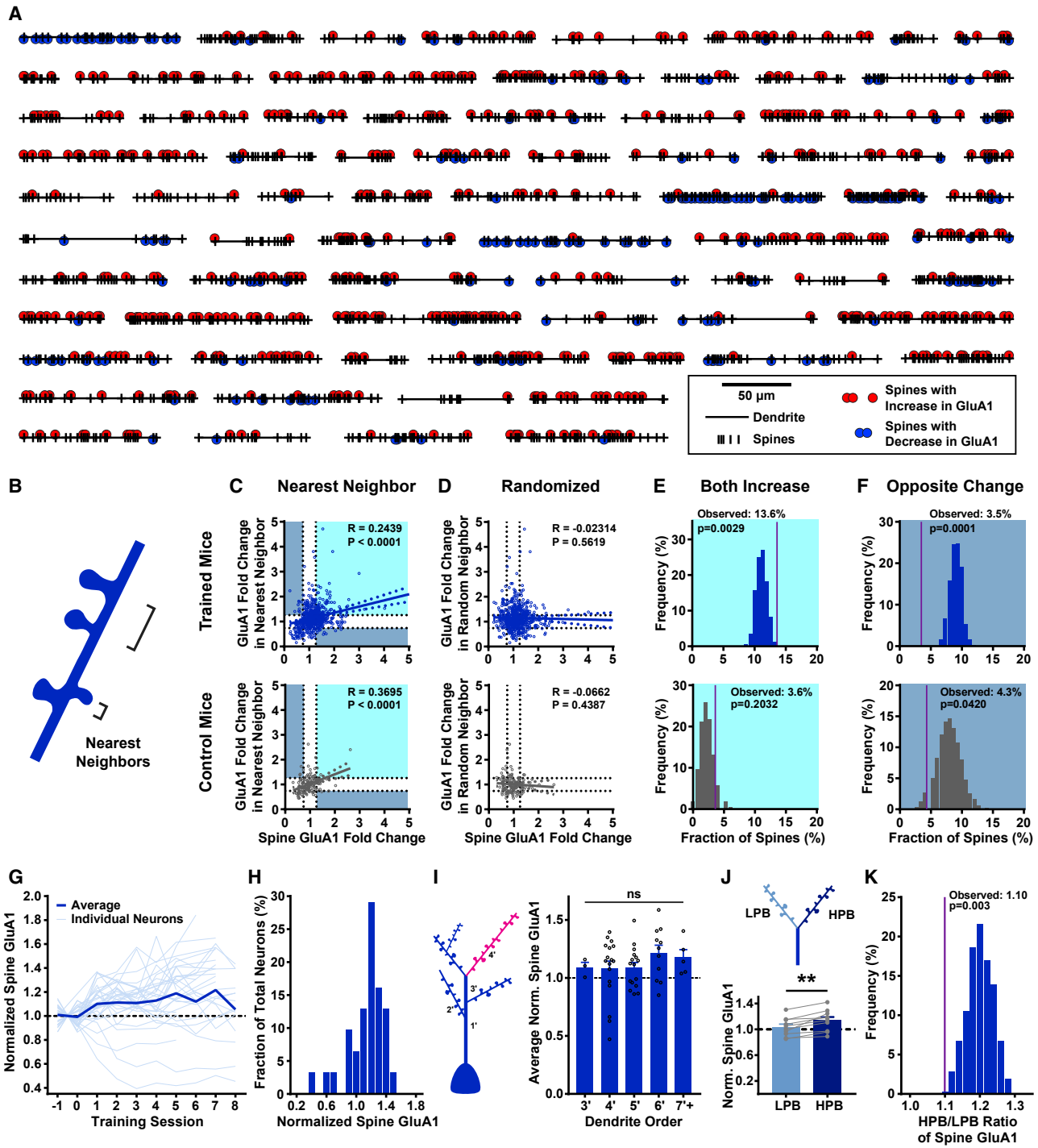


**Figure 4. Spine GluA1 Plasticity is Locally Clustered**

(A) Dendrospinogram of individual dendritic segments from trained mice indicating the location of all spines (black vertical line) along the segment. Location of spines showing an average increase (>26%) in spine GluA1 during learning are indicated in red and spines showing an average decrease (>26%) are indicated in blue.

(B) Schematic drawing of nearest neighbor spines.

(C) Average changes in spine GluA1 intensity during learning in neighboring spines in trained mice (top) and control mice (bottom) with linear fits. Changes in spine sGluA1 intensity in the same direction in neighboring spines are highlighted in turquoise (both spines increase > 26%), and changes in spine sGluA1 intensity in opposite directions in neighboring spines are highlighted in dark blue (one spine increases > 26%, one spine decreases > 26%). Dashed horizontal lines: left, 0.74, right, 1.26. Dashed vertical lines: upper, 1.26, lower, 0.74. n = 631 spine pairs (trained), n = 139 spine pairs (control).

(legend continued on next page)

driven by a subset of spines that progressively enhanced GluA1 expression throughout training.

### Spatial Organization of Spine GluA1 Plasticity

Previous studies have indicated that activity-driven synaptic plasticity can be spatially coordinated at a local level. While nearby synapses can show clustered plasticity changes in the same direction during learning (Fu et al., 2012; Makino and Malinow, 2011) or sensory stimulation (Zhang et al., 2015), they can also change in opposite directions (El-Boustani et al., 2018). When we plotted the spatial distribution of spines along individual dendrites, we noticed local clusters of spines showing either a common increase or decrease in GluA1 levels over the course of motor learning (Figure 4A). We analyzed the local distribution of GluA1 dynamics by comparing changes observed in one spine with changes in its nearest neighbor (Figure 4B). We found that in trained mice, there was a positive correlation in GluA1 changes between two neighboring spines (Figure 4C, top), whereas no correlation was found in a randomized spine pairing (Figure 4D, top). In 13.6% of all spine pairs, both spines showed an increase (upper right quadrant in Figure 4C, top), which was significantly higher than in a distribution of randomly paired spines (Figure 4E, top). Only 3.5% of all spine pairs showed changes in opposite directions (upper left and lower right quadrant in Figure 4C, top) which was significantly lower than in a distribution of randomly paired spines (Figure 4F, top). Although changes in GluA1 levels of nearest neighbors in control mice were also positively correlated (Figure 4C, bottom), the number of spine pairs with both spines increasing (3.6%) was not significantly different from a distribution of randomly paired spines (Figures 4D–4F, bottom). This suggests that basal fluctuations of spine AMPAR levels in control mice are randomly distributed, whereas the learning related increase in spine AMPARs is spatially clustered along dendrites.

Since not all spines showed the same increase in GluA1 we observed on average, we wondered whether all neurons in a mouse showed the same increase, or whether there is also diversity in AMPAR plasticity between neurons. To identify which neuron a spine belonged to, we imaged larger volumes at the end of training in a subset of mice and traced their dendritic tree. In total, we identified 34 individual neurons with on average 2 dendritic segments imaged. The majority of neurons showed a gradual increase in average GluA1 levels of their spines, but the

degree of increase varied between individual neurons, and some neurons also showed an average decrease or no change in GluA1 levels following learning (Figures 4G and 4H).

We further examined whether all dendritic segments along a single neuron showed the same change in spine GluA1 levels and found that some segments showed an increase in spine GluA1 levels, whereas others didn't change or showed a decrease. The dendritic segment order of a given segment did not seem to predict whether that segment would show an increase or decrease in spine GluA1 levels (Figure 4I). However, there was a small trend toward higher order dendritic segments showing larger increases. Since it has been previously reported that sibling dendrites, which are two segments of the dendritic tree that share the same branch point, show different levels of spine turnover during motor learning (Yang et al., 2014), we decided to examine whether AMPAR dynamics were also different between sibling dendrites. Indeed, we found that when we categorized sibling dendrite pairs into a high plasticity branch (HPB) and a low plasticity branch (LPB), on average the high plasticity branches showed a significantly larger increase in spine GluA1 (~10%) during motor learning compared to the low plasticity branches (Figure 4J). However, when we looked at randomized pairings of dendritic branches, we found that the expected ratio of increases within pairs would be even larger, with a distribution centered around 20% (Figure 4K). Thus, while there was diversity in GluA1 level changes during learning among dendritic segments of the same neuron, the difference between sister branches within a neuron was significantly lower than the difference between two branches from separate neurons.

### Motor Learning Induced Spine GluA1 Plasticity in Visual Cortex

Though earlier studies have shown that mice learning the forelimb reaching task show plasticity specifically in the motor cortex contralateral to the trained paw (Guo et al., 2015; Harms et al., 2008; Rioult-Pedotti et al., 1998; Xu et al., 2009), more recent studies have demonstrated that multiple regions of the cortex are activated when mice perform motor tasks such as reaching or licking (Allen et al., 2017; Makino et al., 2017). Thus, we decided to investigate whether training on the forelimb reaching task affects AMPAR dynamics in cortical regions other than the motor cortex. We trained mice and imaged spine AMPARs in

(D) Same as (C) with randomized spine pairing.

(E) Distribution of fraction of spine pairs where both spines increase from 10,000 random spine pairings. Magenta vertical line marks the observed fraction of spines (13.6% for trained mice [top] and 3.6% for control mice [bottom], see (C)). Monte Carlo p value was calculated by summing the tail of the shuffled histogram.

(F) Distribution of fraction of spine pairs where spines show changes in opposite directions from 10,000 random spine pairings. Magenta vertical line marks the observed fraction of spines (3.5% for trained mice (top) and 4.3% for control mice (bottom), see C). Monte Carlo p value was calculated by summing the tail of the shuffled histogram.

(G) Average spine GluA1 levels of all dendritic segments within individual neurons (light blue) and average of all neurons (dark blue) over the course of motor learning.

(H) Distribution of average neuronal spine GluA1 levels during motor learning.

(I) Left: schematic of neuronal tracing to identify dendrite order. Dendrite in magenta exemplifies 4' dendrite. Right: average spine GluA1 levels during motor learning in dendritic segments of different orders. Error bars, SEM ns, not significant, one-way ANOVA.

(J) Top: separation of two sibling dendritic branches into a low plasticity branch (LPB, light blue) and high plasticity branch (HPB, dark blue) based on average spine GluA1 change during motor learning. Bottom: within sibling branch pairs average spine GluA1 is significantly higher in HPB compared to LPB. Gray lines, individual branch pairs. n = 10 branch pairs. Error bars, SEM. \*\*p < 0.01, paired t test.

(K) Distribution of mean ratio between spine GluA1 levels in HPB and LPB in 10,000 times randomly paired dendritic segments. Observed mean ratio difference (J) was 1.1. p = 0.003.

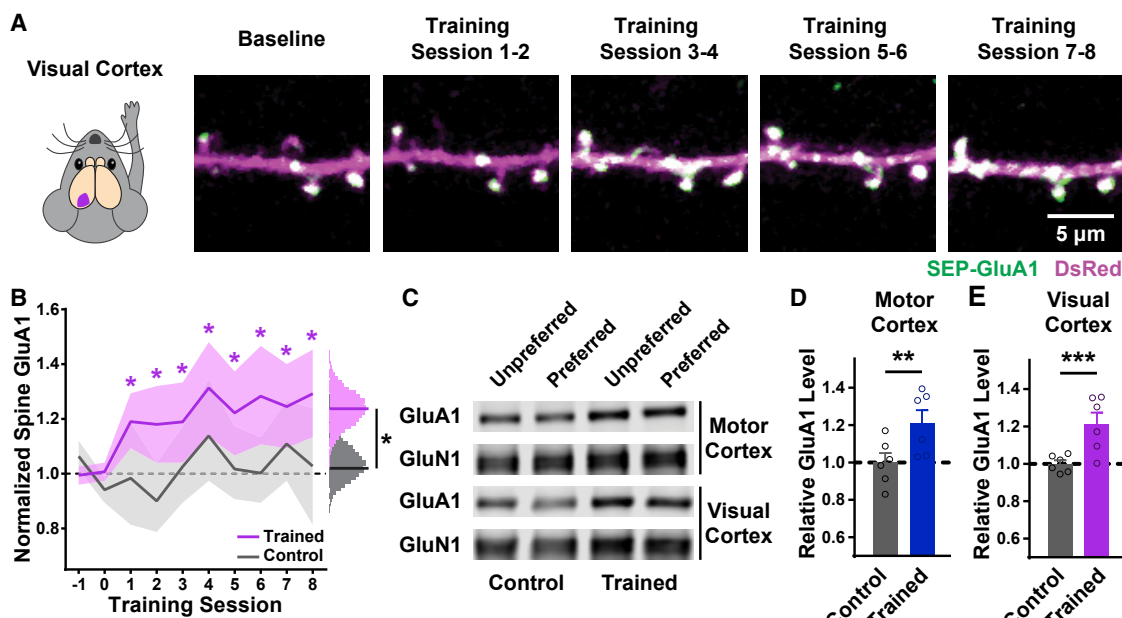


**Figure 5. Increased Spine GluA1 Levels in the Visual Cortex during Motor Learning**

(A) Representative images of spines on layer 5 apical dendrites in the visual cortex of trained mice over the course of motor training.

(B) Average spine GluA1 intensity normalized to baseline levels in the visual cortex of trained mice (magenta) over the course of motor training and in the visual cortex of control mice (gray).  $n = 14$  dendrites with 251 spines from 4 mice (trained) and  $n = 10$  dendrites with 154 spines from 3 mice (control). Line represents averages, shading depicts bootstrapped 95% confidence intervals (see STAR Methods). \* $p < 0.05$  indicates significant difference of mean fluorescence signal intensity from baseline. Right histograms represent distribution of bootstrapped mean values during training. \* $p < 0.05$  indicate significant mean difference between groups.

(C) Immunoblots of PSDs from motor cortex and visual cortex of control and trained mice.

(D) Quantification of synaptic GluA1 normalized to GluN1 in the motor cortex (bilateral average) of trained and control mice.  $n = 6$  each. Error bars, SEM. \*\* $p < 0.01$ , unpaired t test.

(E) Quantification of synaptic GluA1 normalized to GluN1 in the visual cortex (bilateral average) of trained and control mice.  $n = 6$  each. Error bars, SEM. \*\*\* $p < 0.001$ , unpaired t test.

layer 5 neurons of the visual cortex (Figure 5A) and indeed detected significant increases in average spine GluA1 levels during motor learning (Figure 5B).

To confirm these results with an independent approach, we trained non-transfected wild-type mice on the forelimb reaching task and micro-dissected different regions of the cortex following the last day of training. We performed biochemical fractionation, extracted post-synaptic densities (PSDs) from these samples, and examined the expression levels of endogenous AMPARs in the PSD by immunoblotting (Diering et al., 2017). Echoing the results obtained with *in vivo* two-photon imaging, we found that in both the motor cortex contralateral and ipsilateral to the trained paw, GluA1 levels in the PSD were increased by 21% compared to untrained control mice (Figures 5C and 5D). Immunoblotting of PSD samples from the visual cortex also showed a similar bilateral increase in GluA1 levels (21%) in trained mice compared to untrained control mice (Figures 5C and 5E).

#### Reduced Synaptic GluA1 Plasticity in Visual Cortex of Mice Trained in Darkness

Previous studies have shown that the sensory and ipsilateral motor regions we imaged did not show any plasticity related

to motor learning (Rioult-Pedotti et al., 1998; Xu et al., 2009) and were dispensable for performing reaching tasks (Guo et al., 2015). We therefore wondered what caused the increase in AMPAR levels in the visual cortex. Since spine GluA1 levels did not increase during baseline imaging, and GluA1 levels in the visual cortex of non-trained control mice were not changed (Figure 5B), this increase was not likely due to exposure to the novel environment of the training chamber. We then hypothesized that the increase in AMPAR levels might reflect either a nonspecific cortex-wide synaptic potentiation as a result of increased attention or motivation during learning, or specific involvement of these sensory senses during task acquisition. To test how sensory information is involved in the forelimb reaching task, we tested whether mice were able to learn the task without visual input. To avoid any compensatory plasticity resulting from long-term sensory deprivation, we acutely deprived mice of visual input during each training session by performing the training in a dark box under infrared (IR) illumination and monitored reaching performance using an IR camera (Figure 6A). We found that mice were able to learn the reaching task to the same degree and showed a similar learning curve as mice trained in the same dark box with white-light illumination (Figure 6B). We next examined whether

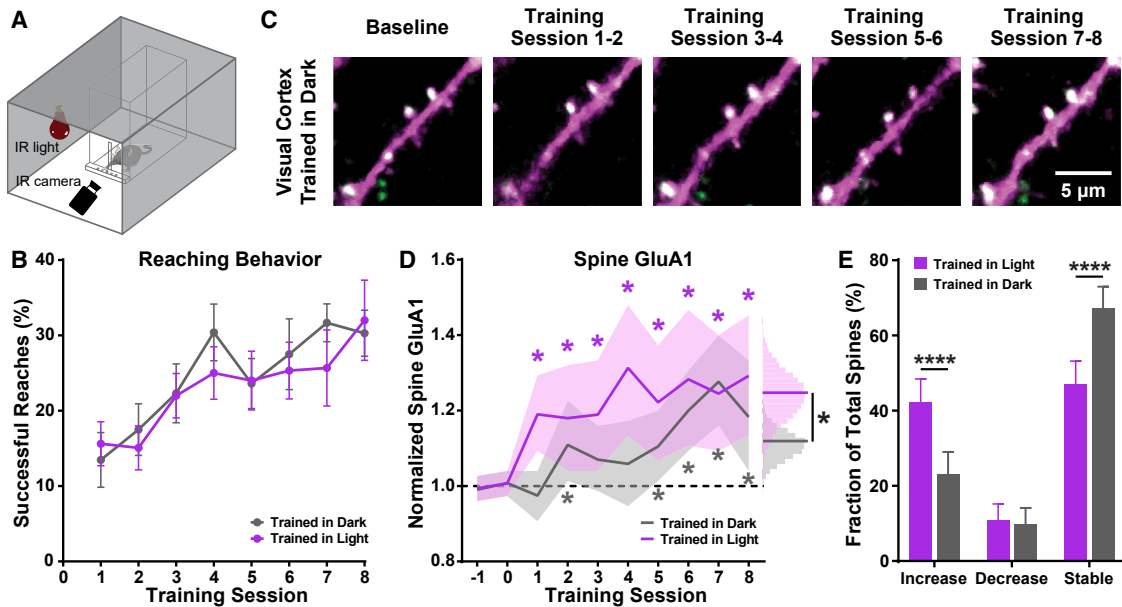


**Figure 6. Training Mice in Darkness Reduces Spine GluA1 Plasticity**

(A) Schematic of mouse trained on forelimb reaching task in darkness with IR light illumination.  
(B) Behavioral performance of mice trained on forelimb reaching task in light (magenta) or dark (gray) conditions.  $n = 10\text{--}12$  mice. Error bars, SEM. No significant difference between groups, repeated-measure two-way ANOVA.  
(C) Representative images of spines on layer 5 apical dendrites in the visual cortex of mice trained in darkness over the course of motor training.  
(D) Average spine GluA1 intensity normalized to baseline levels in mice trained under light (magenta, same as Figure 5B) and mice trained in darkness (gray) over the course of motor learning. Line represents average across  $n = 14$  dendrites with 251 spines from 4 mice (trained in light) and  $n = 13$  dendrites with 229 spines from 4 mice (trained in dark). Shading depicts bootstrapped 95% confidence intervals (see STAR Methods). \* $p < 0.05$  indicates significant difference of mean fluorescence signal intensity from baseline. Right histograms represent distribution of bootstrapped mean values during training. \* $p < 0.05$  indicate significant mean difference between groups.  
(E) Fraction of spines showing an average increase (>26% increase over baseline), decrease (>26% decrease), or are stable (<26% change) during learning. Error bars, 95% confidence intervals. \*\*\* $p < 0.0001$ , chi-square test with Bonferroni correction.

spine GluA1 dynamics in dark-trained animals were different from mice trained in light. Using *in vivo* two-photon imaging of SEP-GluA1, we found that training induced increases in spine GluA1 levels in the visual cortex of dark-trained mice were significantly lower than in light-trained mice (Figures 6C and 6D). This difference resulted from a reduction in the fraction of spines that increased in their GluA1 levels during learning (Figures 6E and S7). Only a small delayed increase in GluA1 levels remained in dark-trained mice, indicating that visual input during learning is mainly responsible for the early increase in average spine GluA1 levels in the visual cortex.

#### Optogenetic Inhibition of Visual Cortex Impairs Reaching Performance of Mice Trained in Light

Since mice were able to learn the motor reaching task in the absence of visual input and the strong increase in visual cortex spine GluA1 levels was only present in mice trained in light, we hypothesized that mice might be using different learning strategies either engaging the visual cortex, or not, depending on the availability of visual information during learning. To functionally test this hypothesis, we trained mice on the task, and then tested their performance while briefly inhibiting specific regions of the brain during reaching. We used mice that expressed Channelrhodopsin2 in inhibitory neurons (VGAT-ChR2 mice) and attached

a headcap on top of a clear skull (Guo et al., 2015, 2014), which allowed us to place optic fibers bilaterally either over the motor cortex or over the visual cortex (Figure 7A). Using this optogenetic approach, we were able to selectively inhibit either the motor cortex or visual cortex (Figure 7B).

We first trained these mice on the forelimb reaching task without inhibition until they were performing at a similar level as previous experiments. In these fully trained mice, we randomly inhibited either motor or visual cortex during two additional training sessions (Figure 7C). To avoid rapid adaptation to optogenetic inhibition, only one-third of trials on a given day were inhibited. We first compared the success rate of reaches with and without motor cortex inhibition in mice trained under normal light conditions. As previously shown in a head-fixed reaching task (Guo et al., 2015), inhibiting the motor cortex during the reach arrested the paw movement, which in all observed trials led to a failure to grab and retrieve the food pellet (Figure 7D). When inhibiting the visual cortex, we also observed an almost complete loss of the ability to successfully retrieve the food pellet. Rather than stopping the paw movement, mice still finished the reaches in these visual cortex inhibition trials, but either missed the pellet or dropped it. To exclude the possibility that blue light from the optic fiber simply distracts mice during reaching, in a separate training session we placed the optic fiber

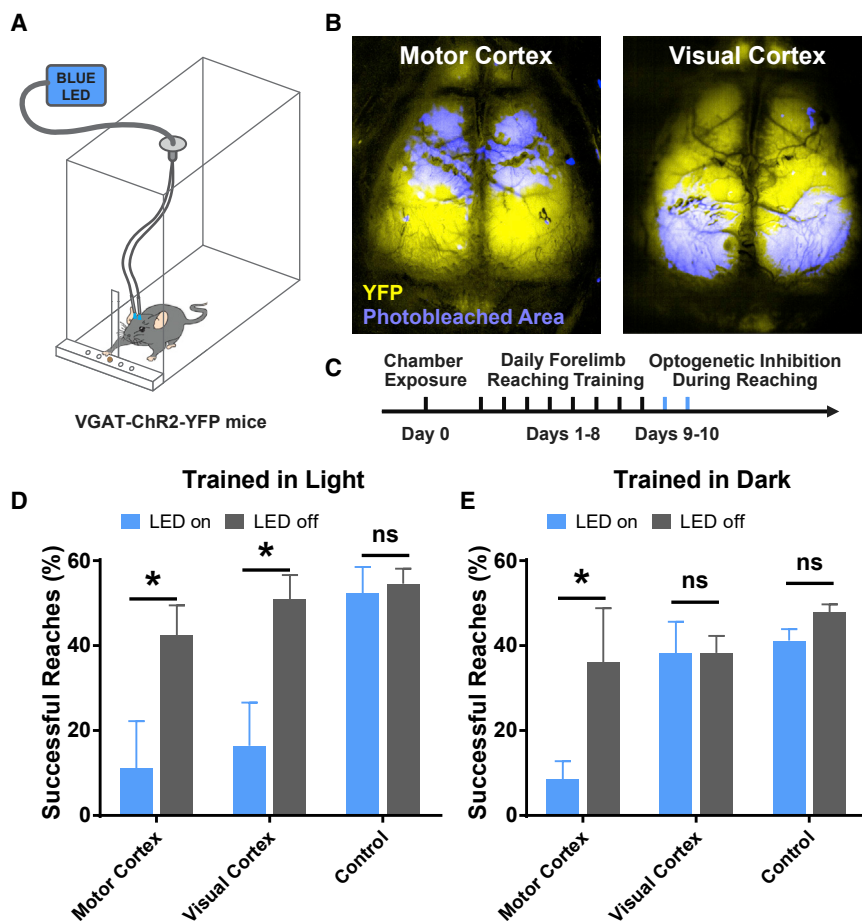


**Figure 7. Training Mice in Darkness Dissociates Visual Cortex from Reaching Performance**

(A) Schematic of mouse trained on forelimb reaching task with bilateral optogenetic fiber implanted on top of cortex.

(B) Wide-field brain imaging of cortex in VGAT-ChR2-YFP mice with photobleaching of regions targeted for optogenetic inhibition.

(C) Experimental timeline for mouse training with two additional behavior sessions on days 9 and 10 (blue) during which in a subset of trials either the motor or visual cortex was optogenetically inhibited.

(D) Reaching performance of mice trained in light comparing trials with (blue) or without (gray) optogenetic inhibition of motor or visual cortex or with the optic fiber placed in the training chamber (control). n = 3 mice each. Error bars, SEM. \*p < 0.05, repeated-measure two-way ANOVA, ns, not significant.

(E) Reaching performance of mice trained in darkness comparing trials with (blue) or without (gray) optogenetic inhibition of motor or visual cortex. n = 3 mice each. Error bars, SEM. \*p < 0.05, ns, not significant, repeated-measure two-way ANOVA.

directly over the slit opening of the training chamber and activated the light in a random subset of reaching trials. Undirected delivery of blue light did not have an effect on the reaching performance, and mice were able to reach with a similar success rate as without blue light (Figure 7D). These results support the idea that mice were indeed using visual cortex to perform the reaching task when visual information was available. We next tested the effects of motor or visual cortex inhibition in mice that were fully trained under dark, IR-lit conditions. As with mice trained in normal light, inhibiting the motor cortex during a subset of trials significantly reduced the reaching performance. However, inhibiting the visual cortex in these mice did not impair their ability to successfully reach (Figure 7E), indicating that dark-trained mice do not require the visual cortex to perform the reaching task.

## DISCUSSION

In this study, we visualized AMPAR levels *in vivo* at individual synapses over the course of motor learning and found that learning induced spatially and temporally coordinated increases in surface GluA1 levels at dendritic spines in the motor cortex. This increase was correlated with increased reaching performance during learning and was maintained after the end of

training. Unexpectedly, spine GluA1 levels in the visual cortex also showed a similarly strong increase during motor learning. The addition of AMPARs to spines in the visual cortex was dependent on visual input during learning: mice trained in the dark did not require visual

cortex activity for task performance, whereas mice trained in ambient light were impaired in the task when visual cortex was inhibited.

Our data provide the most detailed and functionally relevant observation of AMPAR synaptic plasticity *in vivo* to date. As AMPARs mediate the majority of fast excitatory transmission at glutamatergic synapses in pyramidal cortical neurons, studying their distribution and dynamic trafficking in synapses serves as a powerful tool to track changes in synaptic strength during experience and learning. While previous studies have focused on the formation and elimination of synapses over the course of motor learning, we have now shown that existing synapses are also plastic, with their AMPAR content being dynamically modulated during learning. From a neuronal circuitry point of view, learning can induce rewiring of circuits by adding or eliminating existing synaptic connections as well as strengthen and weaken existing connections. Together, these synaptic changes likely play a role in gating information flow in the motor cortex and influence the changes in neuronal activity patterns described previously in similar motor learning tasks (Peters et al., 2014, 2017a).

The importance of synaptic plasticity at existing spines is further supported by the positive correlation between increases in spine GluA1 levels and improvements in reaching

performance, as well as the observation that these increases were long-lasting. This suggests that postsynaptic potentiation of a subset of dedicated spines is part of a memory trace encoding the learned motor skill. In line with this theory, newly formed spines during learning are long-lasting (Xu et al., 2009; Yang et al., 2009), and selective shrinking of motor-learning-related spines causes a significant reduction in learned motor performance (Hayashi-Takagi et al., 2015).

Interestingly, we did not observe an increase in the fraction of spines that were weakened through a loss of AMPARs throughout learning while previous studies have found that motor learning also induces an increase in the elimination of spines especially at later stages of learning (Peters et al., 2014; Xu et al., 2009). This suggests that modification of existing circuits through AMPAR plasticity and circuit rewiring through spine formation and elimination are playing complementary roles during learning in which existing stable circuits are predominantly strengthened while new connections are formed, and a fraction of existing connections can be removed. Elucidating whether spines that are potentiated are part of the same neuronal circuits that lose or gain spines will be an interesting focus for future studies using tracing experiments to identify presynaptic inputs to these dynamic spines.

The observation of dynamic changes in synaptic strength following learning agrees with the Hebbian theory of activity-dependent synaptic plasticity to strengthen task-relevant neuronal circuits (Hebb, 1949; Malenka and Nicoll, 1993). However, we found that the GluA1 content of individual spines under baseline conditions were also surprisingly dynamic. There has been previous experimental evidence supporting activity-independent synapse remodeling (Cane et al., 2014; Gray et al., 2006; Yasumatsu et al., 2008; Ziv and Brenner, 2018), which suggests that synaptic plasticity is not purely induced by novel learning, but that changes in the molecular composition of synapses and synaptic strength occur constantly. These changes may serve to keep the neuronal circuitry dynamic in order to quickly adapt to new relevant information (Gerrow and Triller, 2010; Rokni et al., 2007).

The spatial organization of spines that show an increase in GluA1 levels during learning is not randomly distributed but, rather, locally clustered, with nearby spines showing changes in the same direction. In contrast, the basal AMPAR dynamics in spines of non-trained control mice are not organized in local clusters. This learning-specific clustering of spine plasticity might reflect locally restricted molecular signaling events driving plasticity and AMPAR trafficking (Colgan et al., 2018; Harvey and Svoboda, 2007) or correlated presynaptic inputs (Bloss et al., 2018; Iacaruso et al., 2017; Toni et al., 1999). Together with previous findings on clustered spine activity and plasticity (Fu et al., 2012; Kleindienst et al., 2011; Makino and Malinow, 2011), our data support the idea of spatially clustered synaptic plasticity that can enhance the effect of activity-dependent, synapse-specific plasticity through non-linear summation of the input signal (Govindarajan et al., 2006; Larkum and Nevian, 2008).

When comparing average changes in GluA1 levels per neuron, we noticed that not all neurons showed the same increase observed in the overall average. The direction and degree to which GluA1 levels change during learning can vary between in-

dividual neurons, with about half of all analyzed neurons showing an increase above the previously defined threshold. Since our imaging approach only covered a small subset of dendritic segments and spines from a given neuron, the diversity in neuron specific responses might be overestimated. However, our observed fraction of task-responsive neurons agrees with previous studies reporting about 50% of all neurons showing motor-task-related activity (Komiyama et al., 2010; Peters et al., 2014).

We further looked at dendritic heterogeneity within these task-engaged neurons and found that sibling pairs of dendrites can show significantly different GluA1 dynamics during learning. This diversity indicates that task-related information might be encoded preferentially in a subset of dendritic segments, leaving other segments open for further plasticity related to a separate task. However, overall differences in GluA1 dynamics between different neurons was higher than between dendritic branches of the same neuron.

The primary motor cortex has been identified as one of the primary sites of neuronal and synaptic plasticity during motor learning. Changes in synaptic strength, spine dynamics, and neuronal firing patterns as well as the necessity of this part of the brain for task execution have been demonstrated during different forms of skilled motor learning in rodents (Peters et al., 2017b; Sanes and Donoghue, 2000; Yu and Zuo, 2011). Interestingly, most studies show that motor-learning-related plasticity is limited to the motor cortex contralateral to the trained paw (Rioult-Pedotti et al., 1998; Xu et al., 2009). However, when we quantified levels of synaptic GluA1 in the ipsilateral motor cortex and visual cortex, we were surprised to see strong increases of over 20% during motor learning, comparable to AMPAR increases we observed in contralateral motor cortex. We were able to confirm these *in vivo* imaging experiments using biochemical methods by isolating synapses from different parts of the brain in trained mice. These results clearly reveal that synaptic plasticity induced by motor learning is more widespread than previously thought, involving multiple cortical regions that represent motor and sensory modalities. Spine GluA1 plasticity in the motor cortex ipsilateral to the trained paw could be explained by the particular execution of the forelimb reaching task in this study. Even though this task is designed to be unidextrous, mice can use the opposing forelimb in a supporting role during the reach and perform a movement sequence involving muscles on both sides of the body. Moreover, mice will use both paws to hold the food pellet while eating. While these movements were not directly the objective of this task, learning can lead to increased proficiency of these bilateral movements, which can be the underlying cause for the increase in GluA1 in the motor cortex ipsilateral to the trained paw. Synaptic plasticity in the sensory regions of the cortex could be explained along similar lines, wherein acquisition of this motor learning task requires visual input (Crochet et al., 2019; Makino et al., 2016; Wolpert et al., 2011). Refinement of the visual sense over the course of training could cause the increase in synaptic AMPAR levels we observed.

The fact that mice are able to learn the forelimb reaching task in total darkness seems to conflict with this hypothesis at first, but further imaging experiments showed that GluA1 plasticity is significantly reduced in mice trained without visual input. This suggests that the strong increase in synaptic GluA1 levels in

the visual cortex depends on the availability of visual input during learning. Accordingly, acute inhibition of the visual cortex during reaching impaired the performance of animals that were trained in light, but not of animals that were trained in dark conditions. Our results suggest that mice can easily adapt to a new learning strategy when one of the senses is not available.

Although learning-related refinement of visual senses and the use of multiple cortical regions can explain a large fraction of our observed AMPAR plasticity, there is still a significant increase in spine GluA1 levels in the visual cortex of mice trained in the dark. Part of this plasticity might be caused by release of neuromodulators such as dopamine, acetylcholine, or norepinephrine. These neuromodulatory systems may be engaged in a cortex-wide manner in response to increased attention and arousal or in anticipation of reward during learning (Hu et al., 2007; Marzo et al., 2009; Rasmusson, 2000; Tritsch and Sabatini, 2012). Synaptic plasticity evoked by this mechanism could be either a side effect of reinforced learning or serve as a gating mechanism for further learning.

In conclusion, we performed longitudinal *in vivo* imaging of synaptic surface AMPARs in the mouse cortex during learning. We have shown that motor learning increases the average levels of spine GluA1 levels in the motor cortex of mice in a spatially and temporally coordinated manner. The degree of GluA1 level changes correlates with the increases in behavioral performance and may serve as a long-lasting synaptic memory trace. Surprisingly, AMPAR plasticity is not only limited to motor regions during motor learning but extends into primary sensory regions such as the visual cortex. Visual input during training drives this plasticity in the visual cortex and engages the visual cortex in the execution of the reaching task. Interestingly, in the absence of visual input, mice flexibly adapt their learning strategy to achieve similar performance rates independent of the visual cortex. Our study reveals that motor learning is a multimodal process requiring widespread cortical synaptic plasticity, but the learning strategy and associated synaptic plasticity can be adapted based on the available sensory input.

## STAR★METHODS

Detailed methods are provided in the online version of this paper and include the following:

- KEY RESOURCES TABLE
- LEAD CONTACT AND MATERIALS AVAILABILITY
- EXPERIMENTAL MODEL AND SUBJECT DETAILS
  - Animals
- METHODS DETAILS
  - *In utero* electroporation
  - Cranial window surgery
  - Mouse behavior
  - *In vivo* two-photon imaging
  - Optogenetic inhibition
  - Slice electrophysiology
  - Slice immunohistochemistry
  - Subcellular fractionation
  - Protein immunoblotting (Western blotting)

## ● QUANTIFICATION AND STATISTICAL ANALYSIS

- Analysis of *in vivo* two-photon imaging data
- Statistics

## ● DATA AND CODE AVAILABILITY

## SUPPLEMENTAL INFORMATION

Supplemental Information can be found online at <https://doi.org/10.1016/j.neuron.2019.12.005>.

## ACKNOWLEDGMENTS

We would like to thank N. Luo, S. Tang, A. Wu, D. Chen, Z. Anderson, W. Amanga, and S. Allen for their assistance with image analysis, M. Ayad for help with immunohistochemistry, and T. Shelley for technical support. We also thank all members of the Huganir laboratory, especially A. Graves and E. Lopez-Ortega, as well as W. Xin for thoughtful comments. This work was supported by the National Natural Science Foundation of China (31771125 to Y.Z.), National Key R&D Program of China (2017YFE0103400 to Y.Z.), Beijing Municipal Science & Technology Commission (Z181100001518001 to Y.Z.), and the National Institute of Health (R01NS036715 and P50MH100024 to R.L.H.).

## AUTHOR CONTRIBUTIONS

R.H.R. and R.L.H. designed experiments. R.H.R. performed imaging and behavioral experiments and analyzed data. H.L.T. and R.H.R. performed and analyzed biochemical fractionation and western blotting experiments. R.H.C. developed image analysis software. I.H. performed and analyzed electrophysiology experiments. Y.Z. provided guidance for imaging experiments. R.H.R. and R.L.H. wrote the manuscript with input from all authors.

## DECLARATION OF INTERESTS

The authors declare no competing interests.

Received: January 15, 2019

Revised: October 30, 2019

Accepted: December 4, 2019

Published: December 31, 2019

## REFERENCES

- Allen, W.E., Kauvar, I.V., Chen, M.Z., Richman, E.B., Yang, S.J., Chan, K., Gradinariu, V., Deverman, B.E., Luo, L., and Deisseroth, K. (2017). Global Representations of Goal-Directed Behavior in Distinct Cell Types of Mouse Neocortex. *Neuron* 94, 891–907.e6.
- Bloss, E.B., Cembrowski, M.S., Karsh, B., Colonell, J., Fetter, R.D., and Spruston, N. (2018). Single excitatory axons form clustered synapses onto CA1 pyramidal cell dendrites. *Nat. Neurosci.* 21, 353–363.
- Bosch, M., and Hayashi, Y. (2012). Structural plasticity of dendritic spines. *Curr. Opin. Neurobiol.* 22, 383–388.
- Bredt, D.S., and Nicoll, R.A. (2003). AMPA receptor trafficking at excitatory synapses. *Neuron* 40, 361–379.
- Cane, M., Maco, B., Knott, G., and Holtmaat, A. (2014). The relationship between PSD-95 clustering and spine stability *in vivo*. *J. Neurosci.* 34, 2075–2086.
- Choquet, D. (2018). Linking Nanoscale Dynamics of AMPA Receptor Organization to Plasticity of Excitatory Synapses and Learning. *J. Neurosci.* 38, 9318–9329.
- Colgan, L.A., Hu, M., Misler, J.A., Parra-Bueno, P., Moran, C.M., Leitges, M., and Yasuda, R. (2018). PKC $\zeta$  integrates spatiotemporally distinct Ca $^{2+}$  and autocrine BDNF signaling to facilitate synaptic plasticity. *Nat. Neurosci.* 21, 1027–1037.

- Crochet, S., Lee, S.H., and Petersen, C.C.H. (2019). Neural Circuits for Goal-Directed Sensorimotor Transformations. *Trends Neurosci.* 42, 66–77.
- Diering, G.H., and Huganir, R.L. (2018). The AMPA Receptor Code of Synaptic Plasticity. *Neuron* 100, 314–329.
- Diering, G.H., Nirujogi, R.S., Roth, R.H., Worley, P.F., Pandey, A., and Huganir, R.L. (2017). Homer1a drives homeostatic scaling-down of excitatory synapses during sleep. *Science* 355, 511–515.
- El-Boustani, S., Ip, J.P.K., Breton-Provencher, V., Knott, G.W., Okuno, H., Bito, H., and Sur, M. (2018). Locally coordinated synaptic plasticity of visual cortex neurons *in vivo*. *Science* 360, 1349–1354.
- Fu, M., Yu, X., Lu, J., and Zuo, Y. (2012). Repetitive motor learning induces coordinated formation of clustered dendritic spines *in vivo*. *Nature* 483, 92–95.
- Gerrow, K., and Triller, A. (2010). Synaptic stability and plasticity in a floating world. *Curr. Opin. Neurobiol.* 20, 631–639.
- Govindarajan, A., Kelleher, R.J., and Tonegawa, S. (2006). A clustered plasticity model of long-term memory engrams. *Nat. Rev. Neurosci.* 7, 575–583.
- Gray, N.W., Weimer, R.M., Bureau, I., and Svoboda, K. (2006). Rapid redistribution of synaptic PSD-95 in the neocortex *in vivo*. *PLoS Biol.* 4, e370.
- Guo, Z.V., Li, N., Huber, D., Ophir, E., Gutnisky, D., Ting, J.T., Feng, G., and Svoboda, K. (2014). Flow of cortical activity underlying a tactile decision in mice. *Neuron* 81, 179–194.
- Guo, J.Z., Graves, A.R., Guo, W.W., Zheng, J., Lee, A., Rodríguez-González, J., Li, N., Macklin, J.J., Phillips, J.W., Mensh, B.D., et al. (2015). Cortex commands the performance of skilled movement. *eLife* 4, e10774.
- Harms, K.J., Rioult-Pedotti, M.S., Carter, D.R., and Dunaevsky, A. (2008). Transient spine expansion and learning-induced plasticity in layer 1 primary motor cortex. *J. Neurosci.* 28, 5686–5690.
- Harvey, C.D., and Svoboda, K. (2007). Locally dynamic synaptic learning rules in pyramidal neuron dendrites. *Nature* 450, 1195–1200.
- Hayashi-Takagi, A., Yagishita, S., Nakamura, M., Shirai, F., Wu, Y.I., Loshbaugh, A.L., Kuhlman, B., Hahn, K.M., and Kasai, H. (2015). Labelling and optical erasure of synaptic memory traces in the motor cortex. *Nature* 525, 333–338.
- Hebb, D.O. (1949). The organization of behavior; a neuropsychological theory (Wiley).
- Henley, J.M., Barker, E.A., and Glebov, O.O. (2011). Routes, destinations and delays: recent advances in AMPA receptor trafficking. *Trends Neurosci.* 34, 258–268.
- Hu, H., Real, E., Takamiya, K., Kang, M.G., Ledoux, J., Huganir, R.L., and Malinow, R. (2007). Emotion enhances learning via norepinephrine regulation of AMPA-receptor trafficking. *Cell* 131, 160–173.
- Huganir, R.L., and Nicoll, R.A. (2013). AMPARs and synaptic plasticity: the last 25 years. *Neuron* 80, 704–717.
- Iacaruso, M.F., Gasler, I.T., and Hofer, S.B. (2017). Synaptic organization of visual space in primary visual cortex. *Nature* 547, 449–452.
- Kessels, H.W., and Malinow, R. (2009). Synaptic AMPA receptor plasticity and behavior. *Neuron* 61, 340–350.
- Kleindienst, T., Winnubst, J., Roth-Alpermann, C., Bonhoeffer, T., and Lohmann, C. (2011). Activity-dependent clustering of functional synaptic inputs on developing hippocampal dendrites. *Neuron* 72, 1012–1024.
- Komiyama, T., Sato, T.R., O'Connor, D.H., Zhang, Y.-X., Huber, D., Hooks, B.M., Gabitto, M., and Svoboda, K. (2010). Learning-related fine-scale specificity imaged in motor cortex circuits of behaving mice. *Nature* 464, 1182–1186.
- Larkum, M.E., and Nevian, T. (2008). Synaptic clustering by dendritic signalling mechanisms. *Curr. Opin. Neurobiol.* 18, 321–331.
- Liao, D., Zhang, X., O'Brien, R., Ehlers, M.D., and Huganir, R.L. (1999). Regulation of morphological postsynaptic silent synapses in developing hippocampal neurons. *Nat. Neurosci.* 2, 37–43.
- Lin, D.-T., Makino, Y., Sharma, K., Hayashi, T., Neve, R., Takamiya, K., and Huganir, R.L. (2009). Regulation of AMPA receptor extrasynaptic insertion by 4.1N, phosphorylation and palmitoylation. *Nat. Neurosci.* 12, 879–887.
- Makino, H., and Malinow, R. (2009). AMPA receptor incorporation into synapses during LTP: the role of lateral movement and exocytosis. *Neuron* 64, 381–390.
- Makino, H., and Malinow, R. (2011). Compartmentalized versus global synaptic plasticity on dendrites controlled by experience. *Neuron* 72, 1001–1011.
- Makino, H., Hwang, E.J., Hedrick, N.G., and Komiyama, T. (2016). Circuit Mechanisms of Sensorimotor Learning. *Neuron* 92, 705–721.
- Makino, H., Ren, C., Liu, H., Kim, A.N., Kondapaneni, N., Liu, X., Kuzum, D., and Komiyama, T. (2017). Transformation of Cortex-wide Emergent Properties during Motor Learning. *Neuron* 94, 880–890.e8.
- Malenka, R.C., and Nicoll, R.A. (1993). NMDA-receptor-dependent synaptic plasticity: multiple forms and mechanisms. *Trends Neurosci.* 16, 521–527.
- Malinow, R., and Malenka, R.C. (2002). AMPA receptor trafficking and synaptic plasticity. *Annu. Rev. Neurosci.* 25, 103–126.
- Marzo, A., Bai, J., and Otani, S. (2009). Neuroplasticity regulation by noradrenaline in mammalian brain. *Curr. Neuropharmacol.* 7, 286–295.
- Matsuzaki, M., Honkura, N., Ellis-Davies, G.C.R., and Kasai, H. (2004). Structural basis of long-term potentiation in single dendritic spines. *Nature* 429, 761–766.
- Miesenböck, G., De Angelis, D.A., and Rothman, J.E. (1998). Visualizing secretion and synaptic transmission with pH-sensitive green fluorescent proteins. *Nature* 394, 192–195.
- Oku, Y., and Huganir, R.L. (2013). AGAP3 and Arf6 regulate trafficking of AMPA receptors and synaptic plasticity. *J. Neurosci.* 33, 12586–12598.
- Peters, A.J., Chen, S.X., and Komiyama, T. (2014). Emergence of reproducible spatiotemporal activity during motor learning. *Nature* 510, 263–267.
- Peters, A.J., Lee, J., Hedrick, N.G., O'Neil, K., and Komiyama, T. (2017a). Reorganization of corticospinal output during motor learning. *Nat. Neurosci.* 20, 1133–1141.
- Peters, A.J., Liu, H., and Komiyama, T. (2017b). Learning in the Rodent Motor Cortex. *Annu. Rev. Neurosci.* 40, 77–97.
- Pologruto, T.A., Sabatini, B.L., and Svoboda, K. (2003). ScanImage: flexible software for operating laser scanning microscopes. *Biomed. Eng. Online* 2, 13.
- Rasmusson, D.D. (2000). The role of acetylcholine in cortical synaptic plasticity. *Behav. Brain Res.* 115, 205–218.
- Rioult-Pedotti, M.-S., Friedman, D., Hess, G., and Donoghue, J.P. (1998). Strengthening of horizontal cortical connections following skill learning. *Nat. Neurosci.* 1, 230–234.
- Rioult-Pedotti, M.-S., Friedman, D., and Donoghue, J.P. (2000). Learning-Induced LTP in Neocortex. *Science* 290, 533–536.
- Rokni, U., Richardson, A.G., Bizzi, E., and Seung, H.S. (2007). Motor learning with unstable neural representations. *Neuron* 54, 653–666.
- Roth, R.H., Zhang, Y., and Huganir, R.L. (2017). Dynamic imaging of AMPA receptor trafficking *in vitro* and *in vivo*. *Curr. Opin. Neurobiol.* 45, 51–58.
- Saito, T., and Nakatsuji, N. (2001). Efficient gene transfer into the embryonic mouse brain using *in vivo* electroporation. *Dev. Biol.* 240, 237–246.
- Sanes, J.N., and Donoghue, J.P. (2000). Plasticity and primary motor cortex. *Annu. Rev. Neurosci.* 23, 393–415.
- Schneider, C.A., Rasband, W.S., and Elceir, K.W. (2012). NIH Image to ImageJ: 25 years of image analysis. *Nat. Methods* 9, 671–675.
- Toni, N., Buchs, P.A., Nikonenko, I., Bron, C.R., and Muller, D. (1999). LTP promotes formation of multiple spine synapses between a single axon terminal and a dendrite. *Nature* 402, 421–425.
- Tritsch, N.X., and Sabatini, B.L. (2012). Dopaminergic modulation of synaptic transmission in cortex and striatum. *Neuron* 76, 33–50.
- Volk, L., Chiu, S.-L., Sharma, K., and Huganir, R.L. (2015). Glutamate synapses in human cognitive disorders. *Annu. Rev. Neurosci.* 38, 127–149.
- Wolpert, D.M., Diedrichsen, J., and Flanagan, J.R. (2011). Principles of sensorimotor learning. *Nat. Rev. Neurosci.* 12, 739–751.

- Xu, T., Yu, X., Perlak, A.J., Tobin, W.F., Zweig, J.A., Tennant, K., Jones, T., and Zuo, Y. (2009). Rapid formation and selective stabilization of synapses for enduring motor memories. *Nature* **462**, 915–919.
- Yang, G., Pan, F., and Gan, W.B. (2009). Stably maintained dendritic spines are associated with lifelong memories. *Nature* **462**, 920–924.
- Yang, G., Lai, C.S.W., Cichon, J., Ma, L., Li, W., and Gan, W.-B.B. (2014). Sleep promotes branch-specific formation of dendritic spines after learning. *Science* **344**, 1173–1178.
- Yasumatsu, N., Matsuzaki, M., Miyazaki, T., Noguchi, J., and Kasai, H. (2008). Principles of long-term dynamics of dendritic spines. *J. Neurosci.* **28**, 13592–13608.
- Yu, X., and Zuo, Y. (2011). Spine plasticity in the motor cortex. *Curr. Opin. Neurobiol.* **21**, 169–174.
- Yudowski, G.A., Puthenveedu, M.A., Leonoudakis, D., Panicker, S., Thorn, K.S., Beattie, E.C., and von Zastrow, M. (2007). Real-time imaging of discrete exocytic events mediating surface delivery of AMPA receptors. *J. Neurosci.* **27**, 11112–11121.
- Zhang, Y., Cudmore, R.H., Lin, D.-T., Linden, D.J., and Huganir, R.L. (2015). Visualization of NMDA receptor-dependent AMPA receptor synaptic plasticity in vivo. *Nat. Neurosci.* **18**, 402–407.
- Ziv, N.E., and Brenner, N. (2018). Synaptic Tenacity or Lack Thereof: Spontaneous Remodeling of Synapses. *Trends Neurosci.* **41**, 89–99.

**STAR★METHODS****KEY RESOURCES TABLE**

REAGENT or RESOURCE	SOURCE	IDENTIFIER
<b>Antibodies</b>		
Rabbit anti-dsRed2	Clontech	Cat# 632496; RRID: AB_10013483
Rat anti-CTIP2	Abcam	Cat# ab18465; RRID:AB_2064130
Goat anti-rabbit Alexa Fluor 568	Thermo Fisher Scientific	Cat # A-11011; RRID:AB_143157
Goat anti-rat Alexa Fluor 647	Thermo Fisher Scientific	Cat # A-21247; RRID:AB_141778
Rabbit anti-GluA1 (JH4294)	Oku and Huganir, 2013	N/A
Rabbit anti-GluN1 (JH2590)	Liao et al., 1999	N/A
Donkey anti-rabbit IgG IRDye 680 conjugate	LI-COR	Cat# 926-32223; RRID:AB_621845
Donkey anti-rabbit IgG HRP conjugate	GE Healthcare Life Sciences	Cat# NA934; RRID:AB_772206
<b>Experimental Models: Organisms/Strains</b>		
Mouse: WT C57BL/6N	Charles River	Strain #027; RRID:IMSR_CRL:027
Mouse: VGAT-ChR2-EYFP, B6.Cg-Tg(Slc32a1-COP4*H134R/EYFP)8Gfng/J	The Jackson Laboratory	Jax # 014548; RRID:IMSR_JAX:014548
<b>Recombinant DNA</b>		
SEP-GluA1	Zhang et al., 2015	N/A
Myc-GluA2	Zhang et al., 2015	N/A
DsRed2	Clontech	Cat# 632406
<b>Software and Algorithms</b>		
MATLAB	Mathworks	<a href="https://www.mathworks.com;">https://www.mathworks.com/</a> ; RRID:SCR_001622
ScanImage	Pologruto et al., 2003	<a href="https://vidriotechnologies.com/">https://vidriotechnologies.com/</a> ; RRID:SCR_014307
IGOR Pro	WaveMetrics	<a href="http://www.waveMetrics.com/products/igorpro/igorpro.htm">http://www.waveMetrics.com/products/igorpro/igorpro.htm</a> ; RRID:SCR_000325
MapManager	Zhang et al., 2015	<a href="https://mapmanager.net">https://mapmanager.net</a>
ImageJ	Schneider et al., 2012	<a href="https://imagej.net/">https://imagej.net/</a> ; RRID:SCR_003070
Prism 8	GraphPad Software	<a href="http://www.graphpad.com">http://www.graphpad.com</a> ; RRID:SCR_002798
Illustrator	Adobe	<a href="https://www.adobe.com/products/illustrator.html">https://www.adobe.com/products/illustrator.html</a> ; RRID:SCR_010279

**LEAD CONTACT AND MATERIALS AVAILABILITY**

This study did not generate new unique reagents. Further information and requests for resources and reagents should be directed to and will be fulfilled by the Lead Contact, Richard L. Huganir ([rhuganir@jhmi.edu](mailto:rhuganir@jhmi.edu)).

**EXPERIMENTAL MODEL AND SUBJECT DETAILS****Animals**

All animals were treated in accordance with the Johns Hopkins University Animal Care and Use Committee guidelines. For all experiments, animals were kept on a 12 h:12 h light/dark cycle. All behavioral and imaging experiments were performed at similar times of day to avoid circadian and sleep related effects. Most experiments were performed using male and female adult (2 – 4 months) WT C57BL/6N mice (Charles River). For optogenetic inhibition experiments, male VGAT-ChR2-EYFP transgenic mice, B6.Cg-Tg(Slc32a1-COP4\*H134R/EYFP)8Gfng/J (Jackson Laboratory) were used. Following cranial window surgery and over the course of behavioral and imaging experiments mice were single housed.

## METHODS DETAILS

### ***In utero* electroporation**

Cortical layer V neurons in the mouse cortex were transfected with SEP-GluA1, myc-GluA2, and dsRed2 (4:2:1) by targeted *in utero* electroporation in E13 embryos as previously described (Saito and Nakatsui, 2001; Zhang et al., 2015). GluA1 tagged with a pH-sensitive form of GFP (Super Ecliptic pHluorin (SEP)) specifically visualizes surface inserted GluA1; GluA2 was included to approximate the endogenous GluA1/GluA2 ratio in transfected neurons; dsRed2 serves as a morphology marker for transfected neurons. Protein expression was driven by a CAG promotor. Following anesthesia with Avertin and laparotomy, the DNA plasmid mixture (0.5–1 µl) was injected into the lateral ventricle of embryos using a pulled-glass pipette. Electroporation was performed using bipolar tweezer electrodes (CUY650P5, Nepagene, Japan) and a square pulse generator (CUY21, BEX Co, LTD., Japan). Previously established electrode positioning was used to target motor or visual cortex.

### **Cranial window surgery**

At the age of 8–12 weeks a custom cut square 3x3 mm cranial window (#1 coverslip glass) was placed over the left hemisphere of the cortex of previously electroporated mice. Mice were anesthetized using Avertin and the anti-inflammatory drugs Carprofen and Dexamethasone were administered. A craniotomy matching the size of the coverslip was cut using #11 scalpel blades (Fine Science Tools) and the coverslip was carefully placed on top of the dura within the craniotomy without excessive compression of the brain. The window was centered using stereotactic coordinates 2 mm lateral of bregma for motor cortex and 2 mm lateral and 3 mm posterior from bregma for visual cortex. The window and skull were sealed using dental cement (C&B Metabond, Parkell). A custom-made metal head bar was attached to the skull during surgery to fixate the mouse for imaging. Mice were housed individually after surgery and allowed to recover for 2–3 weeks before two-photon imaging.

### **Mouse behavior**

Before onset of training, mice were given restricted access to food over the course of 5–7 days. Daily food access was adjusted for the mice to reach and maintain ~85% of their initial body weight. A week before training all mice were tested for their preferred paw by allowing them to perform 10 reaches for food pellets and the more frequently used paw was determined. Mice were grouped into the contralateral (right paw) and ipsilateral (left paw) imaging group based on their preferred paw since all mice were imaged on the left hemisphere. We did not observe any differences in the behavior between mice trained on their preferred right paw or preferred left paw (Figure S4A–C). Before the first training day, mice were placed in the training chamber for 20 min for a first chamber exposure session with a small amount of food being provided in the chamber. Baseline imaging data was acquired 1–2 h after this chamber exposure session (Imaging Session 0) and the day before chamber exposure (Imaging session –1). During training mice were trained once per day for 8 days. Each training session consists of 30 reaches or 25 min. Mice were imaged 1–2 h after each training session. In a subset of mice, an additional imaging session was taken 24 h after the last training. For reaching memory testing, mice were kept on restricted food access for one additional week after the last training session. At day 15, reaching performance memory was tested again and another image was taken. Control mice underwent similar procedures but were only exposed to the training chamber without training, but were given a similar amount of food pellets in the chamber as the trained mice retrieved. Mice trained in total darkness (Figures 6, 7, and S7) underwent similar food restriction and forelimb reaching training procedures, however the training chamber was placed inside a light-tight dark box with glove access for food pellet placement. The behavior was monitored through an IR camera under IR illumination.

### ***In vivo* two-photon imaging**

*In vivo* images were acquired of mice under Ketamine/Xylazine anesthesia with a custom-built, two-photon laser-scanning microscope controlled by ScanImage written in MATLAB (Pologruto et al., 2003). Apical dendrites of layer V pyramidal neurons were imaged using a 20 × /1.0 NA water-immersion objective lens (Zeiss). SEP-GluA1 and dsRed2 were excited at 910 nm with a Ti:sapphire laser (Coherent) with 15–100 mW of power delivered to the back-aperture of the objective. Image stacks were acquired at 1,024 × 1,024 pixels with a voxel size of 0.12 µm in x and y and a z-step of 1 µm at a pixel dwell time of ~2 ns. Image stacks for reconstruction of the dendritic tree were acquired at 512 × 512 pixels with a voxel size of 0.72 µm in x and y and a z-step of 3 µm. Representative images shown in figures were median filtered and contrast enhanced.

### **Optogenetic inhibition**

For behavioral testing under optogenetic inhibition of either motor or visual cortex, a clear-skull cap with a custom made headpost was surgically attached to VGAT-ChR2-EYFP mice. Mice were anesthetized using Avertin and the anti-inflammatory drugs Carprofen and Dexamethasone were administered. Following removal of scalp and periosteum, a layer of cyanoacrylate adhesive (Zap-A-Gap, Pacer Technology) was applied to the intact skull. After curing of the glue, a custom metal headpost for mounting of optic fibers was attached using additional cyanoacrylate adhesive. Blue light from a 455nm LED (Prizmatix) was guided through a rotary joint and Y-shaped bifurcating optical fiber (core diameter:500 µm, NA: 0.63) to generate two spots on the brain surface with a diameter of 3mm and power of ~5mW/mm<sup>2</sup>.

Following 1-2 weeks of recovery after the surgery, mice were trained on the forelimb reaching task as described above. In well-trained animals two additional behavioral sessions were performed which consisted of a total of 80 reaching trials each. During a random subset (30%) of the first 20 trials blue light stimulation in the training chamber (not targeting the brain) was activated to assess the non-specific effect of blue light on the behavior. In 30% of the following 60 trials either the motor cortex or visual cortex was inhibited during the reach and the outcome of each trial was recorded. Blue light stimulation (40 Hz for 1 s) during reaching trials was controlled using pulse train generator (Pulser Plus, Prizmatix).

To determine regional specificity of optogenetic inhibition, we took advantage of brain-wide EYFP expression in the VGAT-ChR2-EYFP mice and performed photobleaching experiments. Using the same setup as described above, we shined blue light for 10 min at ~7mW/mm<sup>2</sup> onto either motor cortex or visual cortex and compared green fluorescence intensity of the entire cortical surface before and after photobleaching using a fluorescence microscope (Leica M60). Post-bleach images were subtracted from baseline images and subsequently Gaussian filtered and overlaid with baseline images for representation (Figure 7B).

### Slice electrophysiology

Whole-cell patch-clamp recordings were performed to assess the excitatory synaptic function in *in utero* electroporated cortical neurons. For this, we prepared acute coronal brain slices from 2-4 month old mice that were previously electroporated with SEP-GluA1, myc-GluA2, and dsRed2. Mice were anesthetized with isoflurane and decapitated. Brains were removed rapidly and placed in ice-cold cutting solution containing 96 mM NMDG, 2.5 mM KCl, 1.25 mM NaH<sub>2</sub>PO<sub>4</sub>, 25 mM NaHCO<sub>3</sub>, 25 mM D-(+)-glucose, 10 mM MgSO<sub>4</sub>, 0.5 mM CaCl<sub>2</sub>, 96 mM HCl, 20 mM HEPES, 12 mM N-acetylcysteine, 5 mM sodium L-ascorbate, 3 mM sodium pyruvate, 0.01 mM taurine, 2 mM thiourea, and oxygenated with carbogen gas (95% O<sub>2</sub> and 5% CO<sub>2</sub>). Coronal slices (300 µm thick) were cut with a vibratome and were kept in ACSF (125 mM NaCl, 2.5 mM KCl, 2 mM MgCl<sub>2</sub>, 2 mM CaCl<sub>2</sub>, 1.0 mM NaH<sub>2</sub>PO<sub>4</sub>, 26.2 mM NaHCO<sub>3</sub> and 11 mM glucose, oxygenated with carbogen gas (95% O<sub>2</sub> and 5% CO<sub>2</sub>) at 23–25°C until recordings. Slices were placed in a submerged chamber and perfused with ACSF supplemented with 1 µM TTX, 50 µM picrotoxin and 100 µM APV to isolate AMPAR-mediated excitatory synaptic transmission. Targeted whole-cell recordings of dsRed2/SEP-GluA1-positive cortical neurons and neighboring non-transfected pyramidal neurons were made using pipettes of 3-5 MΩ resistance. The intracellular solution contained 115 mM CsMeSO<sub>4</sub>, 0.4 mM EGTA, 5.0 mM TEA-Cl, 1 mM QX314, 2.8 mM NaCl, 20 mM HEPES, 3.0 mM ATP magnesium salt, 0.5 mM GTP sodium salt and 10 mM phosphocreatine disodium salt (pH = 7.2 and osmolality of 285–290 mOsm). Upon achieving whole-cell mode, > 3 min was allowed for dialysis of the intracellular solution before collecting data. Cells were held at –70 mV holding potential and recording was performed at room temperature. The junction potential was left uncorrected. Signals were measured with a MultiClamp 700B amplifier and digitized using a Digidata 1440A digitizer (Molecular Devices). Data were acquired with pClamp 10 software (Molecular Devices) and digitized at 20 kHz. Miniature EPSCs (mEPSCs) were analyzed with MiniAnalysis (Synaptosoft) using a detection threshold of 7 pA (> 2 times root mean square noise). Decay time constants were obtained by single-exponential fitting of the average mEPSC traces. Rise time was measured as the 10%–90% interval of the rising phase of the average mEPSC traces. Paired t tests were used to compare the mEPSC characteristics of transfected and non-transfected neuron pairs.

### Slice immunohistochemistry

Animals were anesthetized with Avertin (0.02ml/g) and then transcardially perfused with phosphate-buffered saline (PBS) and 4% paraformaldehyde (PFA). The brain was removed and post-fixed in 4% PFA/PBS for 2 h. The brain was sectioned coronally into 100 µm thick slices using a vibratome (VT-1000, Leica). Free-floating sections underwent antigen retrieval using L.A.B. solution (Poly-sciences) and were blocked in 1% BSA with 0.3% Triton X-100 in PBS for 1 h at room temperature. Sections were incubated with primary antibodies overnight at 4°C and then with secondary antibodies either for 2 h in room temperature. Washes after the primary and secondary antibody were done in PBS and antibodies were diluted in PBS containing 0.2% BSA. Slices from motor cortex were mounted in PermaFluor mounting medium (Thermo Scientific) and tiled z stack images were obtained using a laser scanning confocal microscope (Zeiss LSM510).

The following primary antibodies were used: rabbit anti-dsRed2 (1:1,000, Clontech) and rat anti-CTIP2 (1:250, Abcam). The following secondary antibodies were used: Alexa Fluor 568 goat anti-rabbit (1:500 Thermo Fisher Scientific) and Alexa Fluor 647 goat anti-rat (1:500 Thermo Fisher Scientific).

### Subcellular fractionation

Micro-dissected cortical tissue was homogenized by passage through a 26 g needle, 12 times, in homogenization buffer [320mM sucrose, 5mM sodium pyrophosphate, 1 mM EDTA, 10 mM HEPES (pH 7.4), 200 nM okadaic acid and protease inhibitors (Roche)]. The homogenate was centrifuged at 800xg for 10 min at 4°C to yield post-nuclear pelleted fraction 1 (P1) and supernatant fraction 1 (S1). S1 was further centrifuged at 17,000 x g for 20 min at 4°C to yield P2 and S2. P2 was resuspended in milliQ water, adjusted to 4 mM HEPES (pH 7.4) from a 1 M HEPES stock solution, and incubated with agitation at 4°C for 30 min. The suspended P2 was centrifuged at 25,000xg for 20 min at 4°C to yield LP1 and LS2. LP1 was resuspended in 50 mM HEPES (pH 7.4), mixed with an equal volume of 1% Triton X-100, and incubated with agitation at 4°C for 15 min. The PSD was generated by centrifugation at 25,000 x g for 20 min at 4°C. The final PSD pellet was resuspended in lysis buffer (PBS containing 50 mM NaF, 5mM sodium pyrophosphate, 1% Nonidet P-40, 1% sodium deoxycholate, 0.02% SDS, 200 nM okadaic acid and protease inhibitors) followed by protein quantification and western blot.

### Protein immunoblotting (Western blotting)

PSD samples were quantified using BCA protein assay kit (Thermo Fisher) and resolved by 8% SDS-polyacrylamide gel electrophoresis (PAGE). Proteins were transferred to PVDF membranes, and the membranes were blocked with Odyssey blocking buffer for 0.5 h at room temperature. Primary antibodies were resuspended in 3% (mass/vol) bovine serum albumin (BSA) in Tris-buffered saline with 0.1% (vol/vol) Tween-20 (TBST) and applied to membranes overnight at 4°C with gentle rocking. After removal of primary antibodies, membranes were washed with TBST and secondary antibodies in TBST were applied for 1 h at room temperature. Blots were washed again and developed using either LI-COR Odyssey CLx Imaging system or Luminata Forte Western HRP substrate (EMD Millipore) and imaged using manual film exposure. The intensity of each protein band on LI-COR images or developed films was background subtracted and measured in LI-COR or ImageJ software. For quantification of synaptic protein levels, GluA1 band intensities were normalized to GluN1 (Figure 5F and 5H) of each sample as loading control. The lack of house-keeping genes such as GAPDH in PSD samples and likely changes of other synaptic proteins such as actin or PSD-95 prevent their use as loading controls in these experiments. These corrected values were further normalized to the average of non-trained control mice to obtain the relative change in synaptic protein levels in trained mice. While samples from the left and right hemisphere were analyzed separately, we did not observe any differences between the hemispheres and used average values of both hemispheres for representation in Figures 5D and 5E.

The following primary antibodies were used: rabbit anti-GluA1 (1:5,000, JH4294, made in house) and rabbit anti-GluN1 (1:500, JH2590, made in house). The following secondary antibodies were used: donkey anti-rabbit IgG IRDye 680 conjugate (1:10,000; LI-COR) and donkey anti-rabbit IgG HRP conjugate (1:10,000; GE Healthcare Life Sciences).

### QUANTIFICATION AND STATISTICAL ANALYSIS

#### Analysis of *in vivo* two-photon imaging data

Signal intensity in dendritic spines was analyzed using the custom software Map Manager (<https://mapmanager.net>) written in Igor Pro (WaveMetrics) as previously described (Zhang et al., 2015). In brief, three dimensional ROIs were defined for each spine, the dendritic shaft adjacent to that spine, and a nearby background region. Spine ROIs were manually defined by the location of the spine tip. For dendritic ROIs the dendritic shaft was first traced using a modified version of the “Simple Neurite Tracer” plugin in ImageJ and subsequently an ROI covering the dendritic shaft for a 4 μm stretch centered on the connection point of the spine. To avoid bias, image analysis was performed by visualizing the dsRed channel only, without seeing SEP-GluA1 signal intensity. To compare intensity values between imaging sessions, the spine SEP-GluA1 or spine dsRed signal was normalized to the dsRed signal on the adjacent dendritic shaft after background subtraction. Since dendritic shaft dsRed expression is overall stable over the experimental time period and on average does not differ between experimental groups, normalizing SEP-GluA1 signal to dendrite dsRed is used to account for small variations in daily imaging conditions (Figure S3).

For all longitudinal comparison of changes in spine or dendrite SEP-GluA1 or spine dsRed, each spine value was normalized to an average of the two baseline imaging sessions, resulting in fold-change values. Unless otherwise stated all average values were first taken across all spines on one dendritic segment and then an average of all dendritic segments per behavioral group was taken. For calculating averages per mouse (Figure S5A-C), all dendritic segments per mice were averaged and subsequently all mice were averaged to obtain group means.

To reduce variability caused by imaging artifacts, such as bleaching or tissue regrowth, we only included spines if the average dsRed pixel intensity values of the spine ROI exceeded 1 standard deviation over the average dsRed pixel intensity values of the spine background ROI. Further, if the dendritic dsRed intensity either varied more 2.5-fold in either direction during baseline sessions or across all imaging sessions during training, the associated spine was excluded from analysis. Lastly, only spines that were existent in at least 5 imaging sessions were included in the analysis. Dendritic segments that contained less than 10 spines after these exclusion criteria were excluded from further analysis.

For comparison of spine GluA1 and behavioral reaching performance (Figure 2B) the slope for normalized spine GluA1 values over time (Figure S5B) and reaching performance (Figure 1C) for each mouse was calculated by linear fitting data points.

Spines were classified as increasing, decreasing, or stable based on their average change in GluA1 levels compared to baseline (Figure 3D and 6E). The threshold for these categories was set based on the variability in non-trained control mice and was defined at baseline ± one standard deviation of GluA1 level changes (±26%). Spines increasing more than 26% during training were classified as increasing, spines decreasing more than 26% were classified as decreasing. Remaining spines were defined as stable. The same thresholds were used to calculate the dynamics in background fluorescence (Figure S6G-I) where the average change in green fluorescence in the spine background region (Figure S3A) was calculated.

Nearest neighbor analysis (Figures 4C-4F) was calculated by finding the closest neighbor of every spine along each dendritic segment. Each nearest neighbor pair was only included once in the dataset and pairs were excluded if their distance was below 1.0 μm (to avoid overlapping ROIs) or above 3.5 μm. The average distance between nearest neighbors was 2.0 μm for trained and control mice.

### Statistics

For testing whether time courses of spine and dendrite GluA1 and spine size are significantly changing over baseline or significantly different between trained and control conditions (Figure 1) or between mice trained in light and dark (Figure 6), we used a bootstrap statistical method. We calculated 10,000 bootstrap replicates of the observed time courses and calculated a mean for each of these samples. Each bootstrap replicate was generated by randomly sampling with replacement from all imaged individual dendritic segments in a condition followed by randomly sampling with replacement from all spines along each segment. Means were calculated as described above for observed data. Using the distribution of these means, we calculated the 2.5<sup>th</sup> and 97.5<sup>th</sup> percentile to represent the 95% confidence intervals that were denoted as gray shaded areas in figures. Significant differences of each time point after baseline from the average baseline value was determined by comparing the baseline value (1.0) with the 95% confidence interval and denoted with “\*” when the 95% confidence interval did not include the baseline value. For calculating confidence interval of group means with averages per mouse (Figure S5A-C), bootstrap replicates were generated by randomly sampling with replacement from all imaged mice of a condition, followed by sampling individual dendritic segments, followed by randomly sampling with replacement from all spines along each segment.

Differences between groups were calculated on the basis of the mean of all imaging sessions during training days. Bootstrapping was performed as described above using the average spine fluorescence intensity values over eight days of training. The distribution of bootstrap means was represented as normalized histograms in the figures. Additionally, for each bootstrap replicate, the ratio difference between two groups was calculated and significance was determined by summing the tails of the bootstrap difference distribution lying beyond the value 1.

All coefficients of correlation were calculated as Pearson correlation coefficient (R) with corresponding p-values.

All further data were presented as mean  $\pm$  SEM (standard error of the mean). Corresponding statistical tests used, statistical significance, and n numbers were indicated in the figure legends.

### DATA AND CODE AVAILABILITY

The *in vivo* imaging datasets and code supporting the current study have not been deposited in a public repository but are available from the corresponding author on request.